Directed flow and global polarization in Au+Au collisions across energies covered by the beam energy scan at RHIC

Ze-Fang Jiang [1,2,*] Xiang-Yu Wu,[2] Shanshan Cao [3,†] and Ben-Wei Zhang[2,4]

[1]*Department of Physics and Electronic-Information Engineering, Hubei Engineering University, Xiaogan, Hubei 432000, China*

[2]*Institute of Particle Physics and Key Laboratory of Quark and Lepton Physics (MOE), Central China Normal University, Wuhan, Hubei 430079, China*

[3]*Institute of Frontier and Interdisciplinary Science, Shandong University, Qingdao, Shandong 266237, China*

[4]*Guangdong Provincial Key Laboratory of Nuclear Science, Institute of Quantum Matter, South China Normal University, Guangzhou, Guangdong 510006, China*

We study the directed flow of identified particles in Au+Au collisions at $\sqrt{s_{NN}} = 7.7$ to 62.4 GeV. The Glauber model is extended to include both a tilted deformation of the QGP fireball with respect to the longitudinal direction and a non-zero longitudinal flow velocity gradient in the initial state. By combining this improved initial condition with a (3+1)-dimensional viscous hydrodynamic model calculation, we obtain a satisfactory description of the transverse momentum spectra and the rapidity dependent directed flow coefficient of different hadron species. Our calculation indicates the sensitivity of the hadron directed flow, especially its splitting between protons and antiprotons, to both the initial geometry and the initial longitudinal flow velocity. Therefore, the combination of directed flow of different hadrons can provide a tight constraint on the initial condition of nuclear matter created in heavy-ion collisions. The initial condition extracted from the directed flow is further tested with the global polarization of Λ and $\bar{\Lambda}$ within the same theoretical framework, where we obtain a reasonable description of these hyperon polarization observed at different collision energies at RHIC.

I. INTRODUCTION

A new state of strongly coupled nuclear matter, known as the quark-gluon plasma (QGP), is created in relativistic heavy-ion collisions at the BNL Relativistic Heavy-Ion Collider (RHIC) and the CERN Large Hadron Collider (LHC) [1–8]. Lattice QCD calculations suggest that the transition from hadronic matter to the QGP is a smooth crossover at zero baryon density [9]. Whether one may obtain a first-order phase transition at finite baryon density by creating compressed baryonic matter (CBM) is still an open question [10]. A first-order transition indicates the existence of a "softest point" in the equation of state (EoS), which may leave a signature in the final state observables such as the transverse collective flow of hadrons [11]. To search for the first-order phase transition, various CBM experiments have been constructed to investigate the QCD phase diagram at high baryon density, such as the Beam Energy Scan (BES) experiment at RHIC [12], as well as experiments at the Nuclotron-based Ion Collider fAcility (NICA) [13], the Japan Proton Accelerator Research Complex for Heavy Ions (JPARC-HI) [14], the Alternating Gradient Synchrontron (AGS) [15,16] at BNL, and the Facility for Antiproton and Ion Research (FAIR) [17]. Various observables have been proposed to seek signals of the first-order phase transition and locate the critical endpoint (CEP)

in the QCD phase diagram, such as higher-order cumulants of conserved charges [18], collective flow of emitted particles [19–23], amplification of the light nuclei multiplicity ratio [24], and even jet quenching in low energy collisions [25,26].

The first-order Fourier coefficient of the azimuthal distribution of particles, known as the rapidity-odd directed flow (v_1) [19,20,27–32], is among the most popular observables in analyzing the QGP properties, considering that they are sensitive to the initial size and geometry of the nuclear matter produced in energetic collisions [1,27,33–44]. Within hydrodynamic models, the directed flow observed in heavy-ion experiments can be understood with an expanding fireball from an initial energy density that is asymmetric (tilted or shifted) with respect to the beam axis. The related phenomenological model calculations provide a reasonable description of the charged particle v_1 measured in Au+Au, Zr+Zr, Ru+Ru, and Pb+Pb collisions [45–50]. However, with zero baryon density, the splitting of v_1 between baryons and antibaryons cannot be explained by the deformed initial energy density distribution alone. It is a great challenge to quantitatively describe the different directed flow coefficients between protons and antiprotons measured at different collision energies in RHIC-BES [19], NA49 [51], and E895 [16] experiments using earlier hydrodynamic and transport models [39,52–56]. Recently, this problem was investigated for Au+Au collisions at the RHIC energies (7.7–200 GeV) by assuming that the baryon density is also counterclockwise tilted [45] or with specific baryon deposition [57–59] in the reaction plane with respect to the longitudinal direction. Therefore, it is of great

*jiangzf@mails.ccnu.edu.cn

†shanshan.cao@sdu.edu.cn

interest to further explore whether this proposal can also be verified at other colliding energies, and whether the corresponding initial geometry of nuclear matter is consistent with other observables such as the global polarization of Λ and $\bar{\Lambda}$ hyperons in heavy-ion collisions.

In this work, we investigate the splitting of directed flow between protons and antiprotons in Au+Au collisions across the BES energies ($\sqrt{s_{NN}} = 7.7$–62.4 GeV) using the (3+1)-dimensional [(3+1)-D] viscous hydrodynamic model CLVisc [60–63]. The 3-D initial condition of the QGP is developed from our earlier study [48] to further include the tilted deformation of the baryon density distribution [45] and the longitudinal flow velocity gradient of the QGP beyond the Bjorken approximation [49,50]. By combining this improved initial condition and the CLVisc model, we are able to provide a satisfactory description of the transverse momentum (p_T) spectra of identified hadrons (π^+, K^+, p, and $\bar{p}$) in different centrality classes of Au-Au collisions at the BES energies. We further show that a simultaneous description of v_1 of pions, protons, and antiprotons relies on the initial geometry of both the medium energy density and the baryon number density, and also the initial longitudinal flow velocity profile. In the end, the medium geometry and longitudinal flow constrained from the rapidity (y) dependence of v_1 is further tested by the global polarization of hyperons, from which the correlation between directed flow and global polarization can be inferred.

The rest of this paper is organized as follows. In Sec. II, we will present our modified Glauber model for initializing the QGP and the CLVisc hydrodynamic model simulation of its further evolution. In Sec. III, we will calculate the transverse momentum spectra, directed flow of identified particles, and global polarization of Λ and $\bar{\Lambda}$ hyperons measured in relativistic heavy-ion collisions at the BES energies, and investigate their dependence on the initial geometry and longitudinal flow of the QGP. In the end, we will summarize and discuss necessary future developments in Sec. IV.

II. MODEL FRAMEWORK

A. Initial condition

We use a modified Glauber model to generate the initial condition of the QGP fireball, which is tilted in the reaction plane of nuclear collisions [47,48,64]. The nuclear thickness function of an incoming nucleus is obtained using the Woods-Saxon (WS) distribution of nucleons as

$$T(x, y) = \int_{-\infty}^{\infty} dz \frac{n_0}{1 + \exp\left(\frac{r - R_0}{d_0}\right)}, \quad (1)$$

where n_0 is the average nucleon density, $r = \sqrt{x^2 + y^2 + z^2}$ is the radial position with x, y, z being the space coordinates, d_0 is the surface diffusiveness parameter, and R_0 is the radius parameter of the nucleus. For Au+Au collision systems at the BES energies (7.7–62.4 GeV), the parameters are listed in Table I.

For two nuclei moving along the beam direction ($\pm\hat{z}$) and colliding with an impact parameter **b**, their corresponding thickness functions can be expressed as

$$T_+(\mathbf{x}_T) = T(\mathbf{x}_T - \mathbf{b}/2), \quad T_-(\mathbf{x}_T) = T(\mathbf{x}_T + \mathbf{b}/2), \quad (2)$$

TABLE I. Parameters of the Woods-Saxon distribution for the Au nucleus [65,66].

Nucleus	n_0 (1/fm^3)	R_0 (fm)	d_0 (fm)
$^{197}_{79}$Au	0.17	6.38	0.535

where $\mathbf{x}_T = (x, y)$ is the transverse plane coordinate. According to the Glauber model, the density distributions of participant nucleons from the two nuclei are then

$$T_1(\mathbf{x}_T) = T_+(\mathbf{x}_T) \left\{ 1 - \left[1 - \frac{\sigma_{NN} T_-(\mathbf{x}_T)}{A} \right]^A \right\}, \quad (3)$$

$$T_2(\mathbf{x}_T) = T_-(\mathbf{x}_T) \left\{ 1 - \left[1 - \frac{\sigma_{NN} T_+(\mathbf{x}_T)}{A} \right]^A \right\}, \quad (4)$$

in which A is the mass number and σ_{NN} is the inelastic nucleon-nucleon scattering cross section [65].

Noncentral collisions deposit energy into the QGP asymmetrically along the longitudinal direction. As illustrated in Fig. 1, a counterclockwise tilt of the medium profile is expected in the reaction plane [46]. This deformation can be introduced into the initial condition of the QGP via a rapidity dependent wounded (or participant) nucleon distribution function as [47,48,67]

$$W_N(x, y, \eta_s) = T_1(x, y) + T_2(x, y)$$
$$+ H_t[T_1(x, y) - T_2(x, y)] \tan\left(\frac{\eta_s}{\eta_t}\right), \quad (5)$$

where the parameter H_t reflects the overall strength of imbalance between the forward and backward spacetime rapidities (η_s), and the function $\tan(\eta_s/\eta_t)$ models the rapidity dependence of this imbalance. A fixed parameter $\eta_t = 8.0$ will be used in the present study, which provides a reasonable description of the directed flow (v_1) of charged particles in our earlier work [48].

The total weight function $W(x, y, \eta_s)$ combines contributions from wounded nucleons and binary collisions as

$$W(x, y, \eta_s) = \frac{(1 - \alpha) W_N(x, y, \eta_s) + \alpha n_{BC}(x, y)}{[(1 - \alpha) W_N(0, 0, 0) + \alpha n_{BC}(0, 0)]|_{\mathbf{b}=0}}, \quad (6)$$

where $n_{BC}(x, y) = \sigma_{NN} T_+(x, y) T_-(x, y)$ is the number of binary (hard) collisions, and $\alpha = 0.05$ is the collision hardness parameter determined by the centrality (or **b**) dependence of the soft hadron yield [61,65].

The energy density $\varepsilon(x, y, \eta_s)$ and the local baryon density at the initial time then read [61,63]

$$\varepsilon(x, y, \eta_s) = KW(x, y, \eta_s) H(\eta_s), \quad (7)$$

$$n(x, y, \eta_s) = \frac{1}{N} W(x, y, \eta_s) H(\eta_s) H_B(\eta_s), \quad (8)$$

in which the overall factor K is determined by the multiplicity distribution ($dN_{ch}/d\eta$ or dN_{ch}/dy) of soft hadrons, N is a normalization factor constrained by the number of participant nucleons, N_{part}.
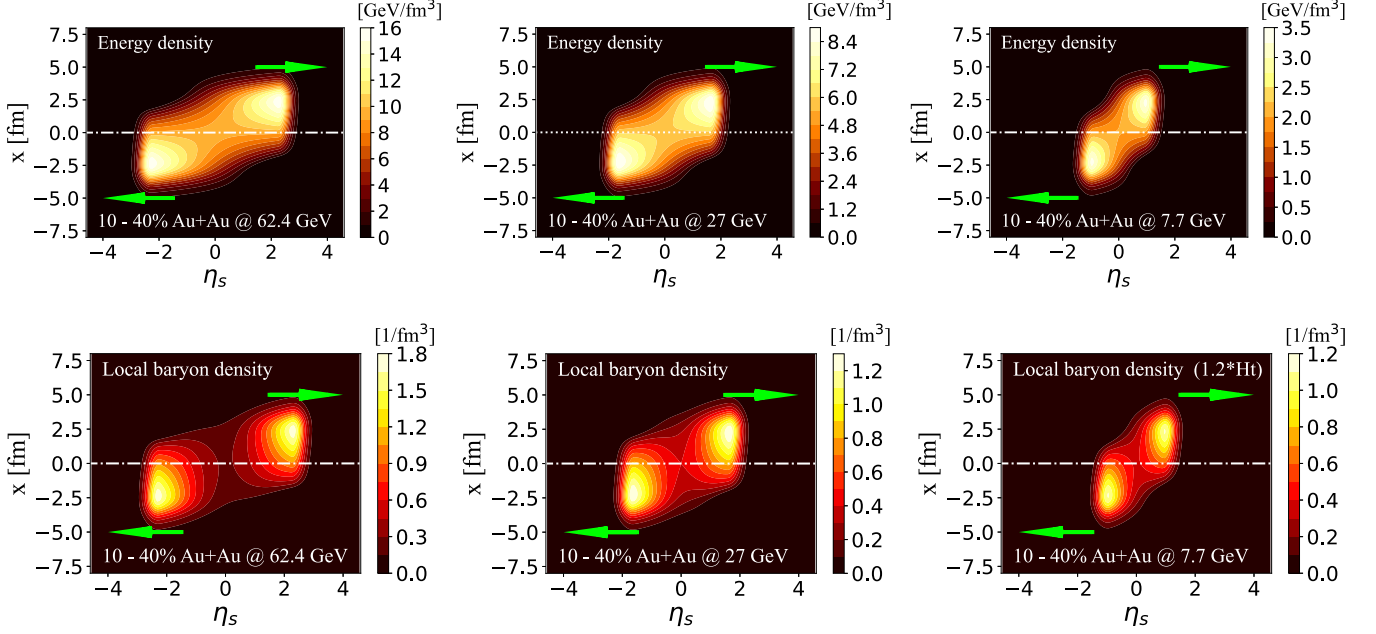
FIG. 1. Distributions of the initial energy density (upper row) and net baryon number density (lower row) on the η_s-x plane for 10–40% Au+Au collisions at $\sqrt{s_{NN}} = 62.4$, 27, and 7.7 GeV. The arrows (lime color) sketch propagation towards the forward and backward rapidity directions.

In Eqs. (7) and (8), a function

$$H(\eta_s) = \exp\left[-\frac{(|\eta_s| - \eta_w)^2}{2\sigma_\eta^2}\theta(|\eta_s| - \eta_w)\right] \quad (9)$$

is introduced to describe the plateau structure of the longitudinal distribution of emitted hadrons, in which η_w controls the width of the central rapidity plateau and σ_η determines the width (speed) of the Gaussian decay outside the plateau region [61]. Following the recent study Ref. [45], the longitudinal dependence of the baryon density is also introduced into the initial condition via

$$H_B(\eta_s) = \exp\left[-\frac{(\eta_s - \eta_n)^2}{2\sigma_n^2}\right] + \exp\left[-\frac{(\eta_s + \eta_n)^2}{2\sigma_n^2}\right], \quad (10)$$

where parameters η_n and σ_n are calibrated by the p_T spectra of protons and antiprotons. This phenomenological ansatz [45] can be qualitatively justified in the string models of the initial state [63,68,69], considering that the titled energy and baryon density profiles originate from strings that connect valence and sea quarks inside nuclei.

Since we aim at understanding the directed flow of soft hadrons and the hyperon polarization within the same framework, the latter of which is sensitive to the gradient of fluid velocity in the longitudinal direction [70], it is necessary to extend the initialization of fluid velocity beyond the Bjorken approximation. Following Refs. [49,50,71], the longitudinal fluid velocity at the initial proper time τ_0 can be given by $v_{\eta_s} = T^{\tau\eta_s}/(T^{\tau\tau} + P)$ with P being the pressure, and the energy-momentum tensor components read

$$T^{\tau\tau} = \varepsilon(x, y, \eta_s) \cosh(y_L), \quad (11)$$

$$T^{\tau\eta_s} = \frac{1}{\tau_0}\varepsilon(x, y, \eta_s) \sinh(y_L), \quad (12)$$

where the rapidity variable is parametrized with

$$y_L \equiv f_v y_{CM}. \quad (13)$$

Here, the center-of-mass rapidity y_{CM} is related to the participant thickness function imbalance as

$$y_{CM} = \text{arctanh}\left[\frac{T_1 - T_2}{T_1 + T_2}\tanh(y_{beam})\right], \quad (14)$$

in which $y_{beam} \equiv \text{arccosh}[\sqrt{s_{NN}}/(2m_N)]$ is the beam rapidity with m_N being the nucleon mass; and $f_v \in [0, 1]$ models the fractional longitudinal momentum attributed to the corresponding flow velocity. This f_v parameter allows us to vary the magnitude of the longitudinal flow velocity, which further affects the slope of the directed flow with respect to rapidity (dv_1/dy) and the global polarization of hyperons. For $f_v = 0$, one has $y_L = 0$, and the velocity field is reduced to the Bjorken flow scenario [49]. The initial fluid velocities in transverse directions are still set as 0 via $T^{\tau x} = T^{\tau y} = 0$, considering that they have little impact on the observables we investigate in this work.

In Table II, we summarize the parameters used for initializing the QGP produced at the BES energies. The first four parameters (K, τ_0, σ_η, and η_w) are adjusted according to rapidity dependence of the charged particle yields (dN_{ch}/dy) in the most central collisions at each colliding energy, and the next two parameters (σ_n and η_n) are from the p_T spectra of protons and antiprotons. The last two parameters (f_v and H_t) are determined by the directed flow of hadrons. Note that since we include both the geometric tilt and the longitudinal velocity in the initial QGP profile, values extracted for f_v in

TABLE II. Parameters for the three-dimensional optical Glauber model of the initial condition of the QGP [49,63].

$\sqrt{s_{NN}}$ (GeV)	K	τ_0 (fm)	σ_η (fm)	η_w	σ_n	η_n	f_v	H_t
62.4	11.8	1.0	0.3	2.25	1.34	2.7	0.18	10.0
39	8.25	1.3	0.3	1.9	1.13	2.1	0.22	13.0
27	7.40	1.4	0.3	1.6	1.06	1.8	0.23	13.5
19.6	5.60	1.8	0.3	1.3	0.85	1.5	0.24	15.5
14.5	3.90	2.2	0.3	1.15	0.81	1.4	0.24	18.0
11.5	3.05	2.4	0.3	1.16	0.79	1.22	0.25	22.0
7.7	2.50	2.6	0.3	0.9	0.70	1.05	0.26	28.0

this work can be different from those in Ref. [50] where only the latter effect is taken into account.

Using these parametrizations, we first present in Fig. 1 the distributions of the energy density (upper row) and net baryon number density (lower row) at τ_0 on the η_s-x plane for 10–40% Au+Au collisions at three different colliding energies ($\sqrt{s_{NN}} = 62.4$, 27, 7.7 GeV). From the figure, one observes that the energy and baryon densities are not only shifted asymmetrically along the forward and backward rapidity directions, but also tilted counterclockwise in the η_s-x plane. Due to different parametrizations between Eq. (7) and Eq. (8), the initial baryon density tends to be shifted towards larger forward and backward rapidity regions than the energy distribution. The asymmetric distribution of baryon density will in the end affect the different abundance between protons and antiprotons at different locations of the QGP fireball [45]. Since a stronger drag on the participant nucleons from spectators is expected at lower collisional energies, we obtain a stronger tilt of the density profile and thus a larger H_t parameter at lower energies. Meanwhile, a larger fractional longitudinal momentum is deposited from the colliding beams into the QGP at lower energies, as reflected by the increasing value of f_v as $\sqrt{s_{NN}}$ decreases. At very low energy (for $\sqrt{s_{NN}} = 11.5$ and 7.7 GeV), we also need to assume the baryon density has a stronger tilt than the energy density by applying $1.2H_t$ for the former, in order to improve our phenomenological description of the proton v_1. This might result from effects of the phase transition [39,53,54,56], emission of the spectator matter [42], and the electromagnetic field [72] that have not been taken into account in our present work.

B. Hydrodynamic evolution

Starting with the initial condition constructed in the previous subsection, we utilize a (3+1)-D viscous hydrodynamic model CLVisc [60–63] to simulate the subsequent evolution of the QGP medium. The hydrodynamic equations read [73–77]

$$\nabla_\mu T^{\mu\nu} = 0, \tag{15}$$

$$\nabla_\mu J^\mu = 0, \tag{16}$$

where the energy-momentum tensor $T^{\mu\nu}$ and the net baryon current J^μ are defined as

$$T^{\mu\nu} = \varepsilon U^\mu U^\nu - P\Delta^{\mu\nu} + \pi^{\mu\nu}, \tag{17}$$

$$J^\mu = nU^\mu + V^\mu, \tag{18}$$

with ε, P, n, u^μ, $\pi^{\mu\nu}$, and V^μ being the local energy density, pressure, net baryon density, flow velocity field, shear stress tensor, and baryon diffusion current respectively. The projection tensor is given by $\Delta^{\mu\nu} = g^{\mu\nu} - u^\mu u^\nu$, with $g^{\mu\nu} = \text{diag}(1, -1, -1, -1)$ being the metric tensor. Effects of the bulk viscosity are not included in the present study yet [49,63,68,78,79].

Based on the Israel-Stewart second-order hydrodynamic expansion, the dissipative currents $\pi^{\mu\nu}$ and V^μ are expressed as follows [79]:

$$\Delta^{\mu\nu}_{\alpha\beta}(u \cdot \partial)\pi^{\alpha\beta} = -\frac{1}{\tau_\pi}(\pi^{\mu\nu} - \eta_v \sigma^{\mu\nu}) - \frac{4}{3}\pi^{\mu\nu}\theta$$
$$- \frac{5}{7}\pi^{\alpha<\mu}\sigma^{\nu>}_\alpha + \frac{9}{70}\frac{4}{e+P}\pi^{<\mu}_\alpha\pi^{\nu>\alpha},$$

$$\Delta^{\mu\nu}(u \cdot \partial)V_\nu = -\frac{1}{\tau_V}\left(V^\mu - \kappa_B\nabla^\mu\frac{\mu_B}{T}\right) - V^\mu\theta - \frac{3}{10}V_\nu\sigma^{\mu\nu}, \tag{19}$$

where $\theta = \partial \cdot u$ is the expansion rate, $\sigma^{\mu\nu} = \partial^{<\mu}u^{\nu>}$ is the shear tensor, and η_v and κ_B are the shear viscosity and baryon diffusion coefficient. For an arbitrary tensor $A^{\mu\nu}$, its traceless symmetric part is given by $A^{<\mu\nu>} = \frac{1}{2}[(\Delta^{\mu\alpha}\Delta^{\nu\beta} + \Delta^{\nu\alpha}\Delta^{\mu\beta}) - \frac{2}{3}\Delta^{\mu\nu}\Delta^{\alpha\beta}]A_{\alpha\beta}$ [63].

In hydrodynamic simulation, the specific shear viscosity C_{η_v} and the baryon diffusion coefficient κ_B are treated as model parameters, which are related to η_v and C_B as

$$C_{\eta_v} = \frac{\eta_v T}{e+P}, \tag{20}$$

$$\kappa_B = \frac{C_B}{T}n\left[\frac{1}{3}\cot\left(\frac{\mu_B}{T}\right) - \frac{nT}{e+P}\right], \tag{21}$$

where μ_B stands for the baryon chemical potential. They connect to the relaxation times as

$$\tau_\pi = \frac{5C_{\eta_v}}{T}, \quad \tau_V = \frac{C_B}{T}. \tag{22}$$

In this work, we set $C_{\eta_v} = 0.08$ and $C_B = 0.4$ for all collision energies.

The hydrodynamic equations are then solved together with the NEOS-BQS equation of state (EOS) [80,81], which is based on the lattice QCD calculation at high temperature and vanishing net baryon density and then extended to finite net baryon density according to the Taylor expansion method [80,81]. It connects the QGP and hadron phases with a smooth crossover under the strangeness neutrality ($n_S = 0$) and the electric charge density $n_Q = 0.4n_B$ conditions.

C. Particlization

The isothermal freeze-out condition [61] is applied in our study, with the freeze-out hypersurface determined by a constant freeze-out energy density ($e_{frz} = 0.4$ GeV/fm^3) [63]. On this hypersurface, the Cooper-Frye formalism is implemented to obtain the momentum distribution of hadrons:

$$\frac{dN}{p_T dp_T d\phi\, dy} = \frac{g_i}{(2\pi)^3}\int_\Sigma p^\mu d\Sigma_\mu f_{eq}(1 + \delta f_\pi + \delta f_V). \tag{23}$$

In the above equation, g_i is the spin-color degeneracy factor for identified hadrons, and $d\Sigma_\mu$ is the hypersurface element determined by the projection method [61]. The thermal distribution ($f_{\rm eq}$) and its out-of-equilibrium corrections (δf_π and δf_V) are given by

$$f_{\rm eq} = \frac{1}{\exp[(p_\mu U^\mu - B\mu_B)/T_{\rm f}] \mp 1}, \qquad (24)$$

$$\delta f_\pi(x,p) = [1 \pm f^{\rm eq}(x,p)]\frac{p_\mu p_\nu \pi^{\mu\nu}}{2T_f^2(e+P)}, \qquad (25)$$

$$\delta f_V(x,p) = [1 \pm f^{\rm eq}(x,p)]\left(\frac{n_B}{e+P} - \frac{B}{U^\mu p_\mu}\right)\frac{p^\mu V_\mu}{\kappa_B/\tau_V}, \quad (26)$$

where $T_{\rm f}$ is the chemical freeze-out temperature and B represents the baryon number of an identified hadron. The out-of-equilibrium corrections above are derived from the Boltzmann equation via the relaxation time approximation [82]. Contributions from resonance decay have been taken into account in this work based on Ref. [61], although hadronic scatterings after the QGP phase has not been included yet.

III. NUMERICAL RESULTS

In this section, we present our numerical results on light hadrons in Au+Au collisions at the BES energies using the (3+1)D CLVisc hydrodynamics model with finite net baryon density and the tilted initial condition. We first present the transverse momentum spectra of identified particles π^+, K^+, p, and $\bar{p}$ in Sec. III A. Then, we study the rapidity dependence of the directed flow of π^+, p, and $\bar{p}$ in Sec. III B. The relation between the slope of v_1 *vs* y and two competing effects—the tilt of the fireball ($H_{\rm t}$) and the fractional longitudinal momentum transferred into the initial flow velocity (f_v)—are investigated in Sec. III C. In the end, we verify the initial condition constrained from the directed flow by reproducing the global polarization of Λ and $\bar{\Lambda}$ hyperons in Sec. III D within the same theoretical framework.

A. Identified particle spectra

We start with validating our model setup by comparing the transverse momentum spectra of the identified light hadrons between our calculation and the STAR data [25] in Fig. 2. As discussed in Sec. II A, the first six model parameters summarized in Table II are adjusted to describe the rapidity dependence of charged particle yields ($dN_{\rm ch}/dy$) and the $p_{\rm T}$ spectra of proton (antiproton) yield in the most central collisions at each colliding energy. With these parameters, the combination of our initial condition and hydrodynamic evolution is able to provide a reasonable description of the $p_{\rm T}$ spectra of different species of identified particles (π^+, K^+, p, and $\bar{p}$) across different centrality bins at these colliding energies. This implies the success of this model setup in describing the bulk evolution of the nuclear matter produced by heavy-ion collisions at the BES energies. More detailed discussions on $p_{\rm T}$ spectra of identified particles, such as their mean $p_{\rm T}$, can be found in Ref. [63], which provides an insight into the radial flow of the QGP medium. This offers a reliable

baseline for our further study of the directed flow coefficient and global polarization.

The last two parameters in Table II (f_v and $H_{\rm t}$) cannot be determined yet, because they control the initial velocity and deformed geometry of the QGP medium, and are insensitive to the integrated particle spectra over the azimuthal angle [45–50,63]. In other words, varying these two parameters according to the directed flow coefficient later will have little impact on the hadron spectra presented in this subsection.

B. Directed flow coefficients of π^+, p, and $\bar{p}$

In this subsection, we study the directed flow coefficients of π^+, p, and $\bar{p}$ in 10–40% Au+Au collisions at the BES energies (7.7–62.4 GeV). As the first-order Fourier component of the azimuthal angle distribution, the directed flow coefficient at a given rapidity can be calculated as

$$v_1(y) = \langle\cos(\phi - \Psi_1)\rangle = \frac{\int \cos(\phi - \Psi_1)\frac{dN}{dy\,d\phi}d\phi}{\int \frac{dN}{dy\,d\phi}d\phi}, \quad (27)$$

where Ψ_1 is the first-order event plane angle of a nucleus-nucleus collision. Since we use a smooth initial condition for the energy density and baryon number density distributions, event-by-event fluctuations are ignored in the present work. Therefore, the event plane here is the same as the spectator plane characterized by the deflected neutrons in experimental measurements. Effects of the initial-state fluctuations on the final-state hadron v_1 will be left for our future exploration.

Shown in Fig. 3 is the directed flow of π^+ as a function of rapidity in 10–40% Au+Au collisions at the BES energies. Here, v_1 is analyzed using soft hadrons within $0 < p_{\rm T} < 3.0$ GeV. One can see that our calculation provides a reasonable description of the pion $v_1(y)$ around midrapidity ($y \in [-1, 1)$) observed at by the STAR Collaboraton [19]. In this work, the directed flow is contributed by two mechanisms: the longitudinally tilted geometry of the QGP medium [Eq. (5)], as discussed in Ref. [47], and the nonzero initial gradient of the longitudinal flow velocity along the direction of the impact parameter ($\partial v_z/\partial x$) [Eqs. (11)–(14)], as proposed in Refs. [49,50,71]. Detailed discussions on how these two effects contribute to the hadron v_1 and how their corresponding model parameters ($H_{\rm t}$ and f_v) are adjusted will be presented later in Sec. III C. In the last two panels for $\sqrt{s_{NN}} = 11.5$ and 7.7 GeV, we also present calculations using a larger tilt parameter ($1.2H_{\rm t}$) for the initial baryon number density distribution. As expected, the pion v_1 is not sensitive to this baryon distribution.

In Fig. 4, we further study the rapidity dependence of v_1 for protons and antiprotons in 10–40% Au+Au collisions at the BES energies. And for a more clear display of this rapidity dependence, its slope is extracted in Fig. 5 around midrapidity ($y \in [-0.5, 0.5]$) as a function of the colliding energy. Consistent with the findings of Ref. [45], extending the tilted initial geometry from energy density to baryon number density leads to a separation of v_1 between protons and antiprotons. Within our model, using the same $H_{\rm t}$ parameter is able to provide a good description of the experiment data when the colliding energy is not very low. However, at $\sqrt{s_{NN}} = 11.5$ and 7.7 GeV,
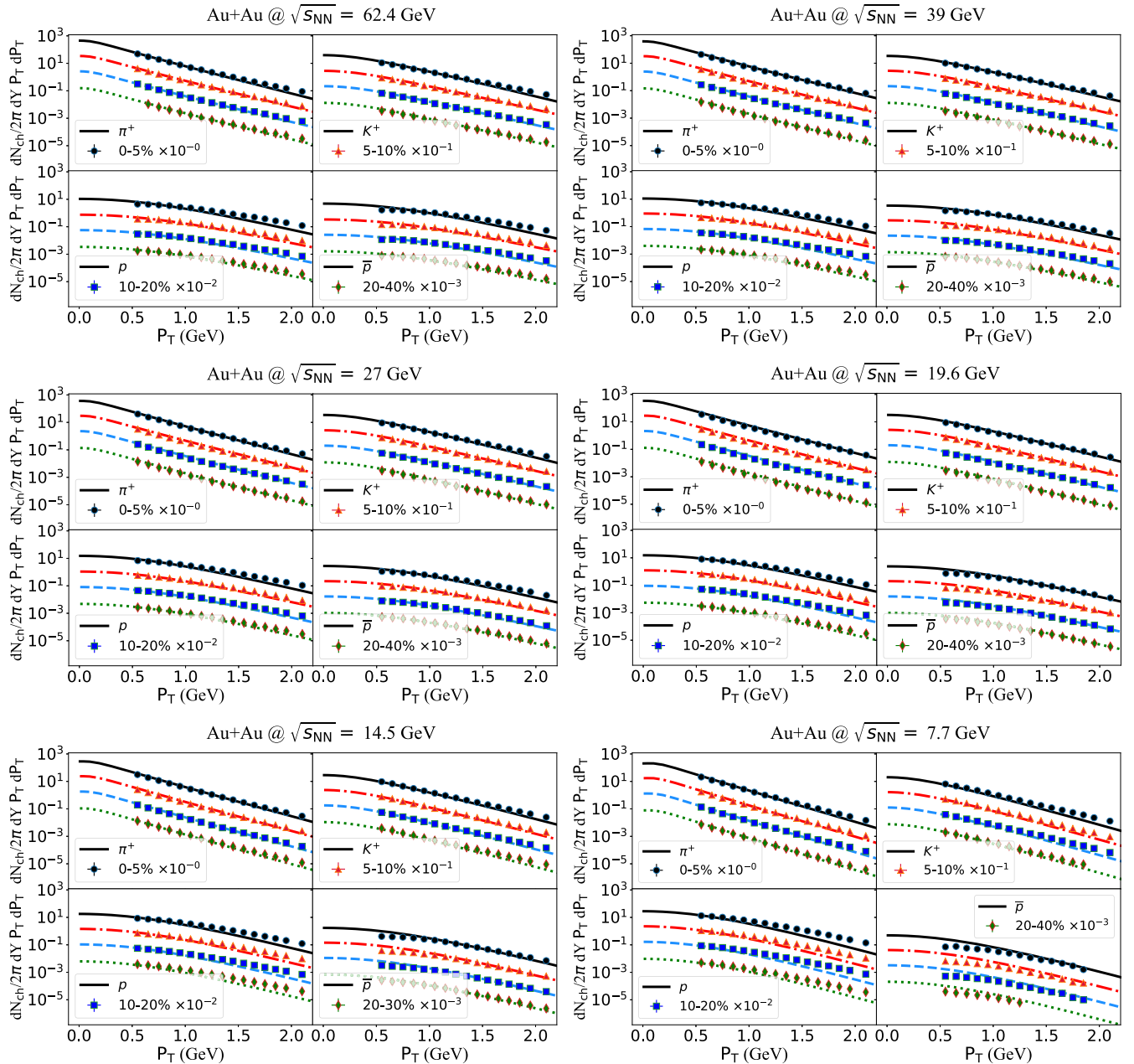
FIG. 2. The transverse momentum spectra of identified charged hadrons (π^+, K^+, p and $\bar{p}$) at mid-rapidity ($|y| < 0.25$) in different centrality classes of Au+Au collisions at $\sqrt{s_{NN}} = 7.7$, 14.5, 19.6, 27, 39 and 62.4 GeV, compared to the STAR data [25].

this minimal assumption seems insufficient. A slightly larger value of H_t for baryon number density than for energy density is required to generate the increasing trend of proton v_1 with respect to y, as well as the splitting between protons and antiprotons observed at very low energies. This larger value of H_t for the baryon density than the overall QGP medium might result from the possible phase transition in the preequilibrium stage [56], the strong electromagnetic field [72], and hadronic scatterings [63].

As shown in Fig. 5, with the increase of colliding energy, the splitting of v_1 between protons and antiprotons becomes

smaller. This can be understood with the weaker tilt of the baryon number density distribution and the slower longitudinal flow velocity in higher energy collisions, and can be confirmed by the increasing values of H_t and f_v extracted in Table II as $\sqrt{s_{NN}}$ becomes smaller. Our calculation indicates the essential role of the geometric distribution of the baryon number density in producing the baryon and antibaryon v_1. It also suggests the necessity of utilizing pions and protons (antiprotons) together to simultaneously constrain both the medium geometry and its longitudinal flow profile.
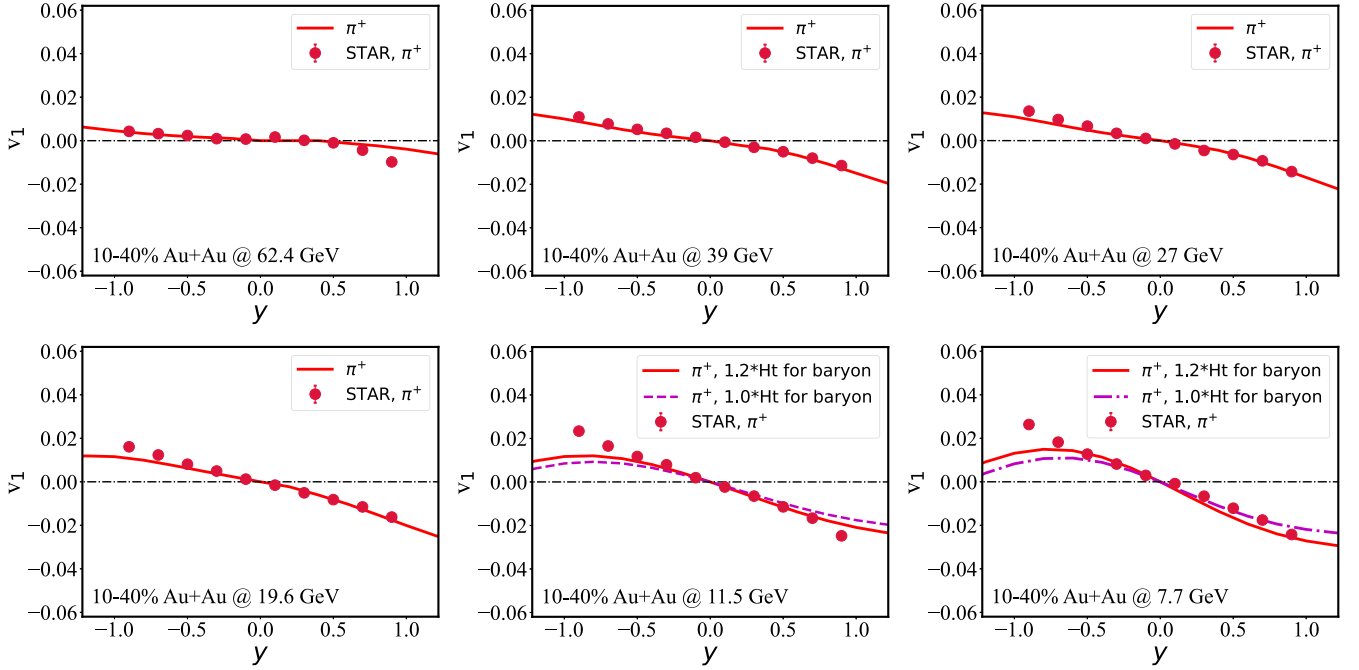
FIG. 3. Rapidity dependence of the directed flow coefficient of π^+ in 10-40% Au+Au collisions at the BES energies, compared between our model calculation and the STAR data [19].

C. Dependence of dv_1/dy on the medium geometry and the longitudinal flow velocity

Both the tilted QGP profile and the longitudinal flow velocity gradient contribute to the directed flow of hadrons in heavy-ion collisions. In this subsection, we investigate how these two effects compete with each other and illustrate how

the two parameters H_t and f_v are determined in our model calculation.

In the upper panel of Fig. 6, we show the slope of the directed flow coefficient dv_1/dy around midrapidity for π^+, proton, and antiproton as a function of the H_t parameter in 10–40% Au+Au collisions at $\sqrt{s_{NN}} = 27$ GeV, while f_v is
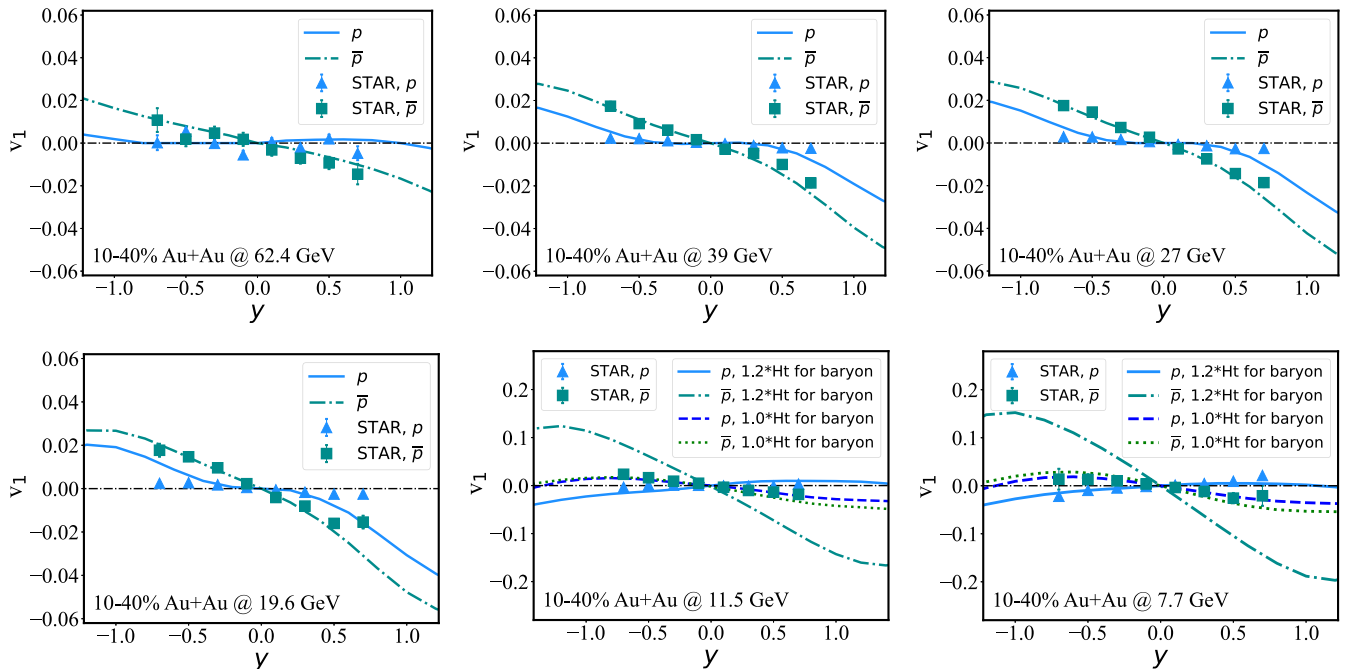

FIG. 4. Rapidity dependence of the directed flow coefficient of protons and antiprotons in 10–40% Au+Au collisions at the BES energies, compared between our model calculation and the STAR data [19].
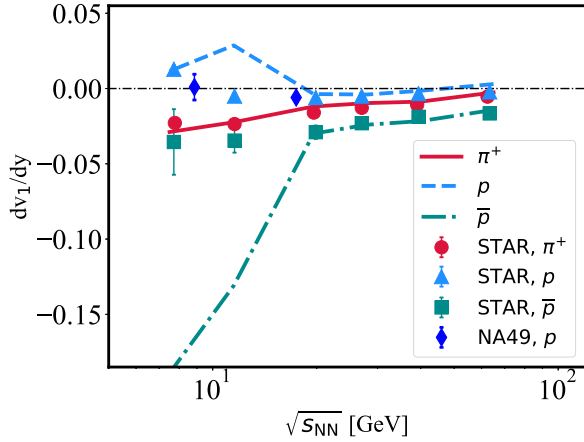
FIG. 5. The slope of the rapidity dependence of the directed flow coefficients of pions, protons, and antiprotons as functions of the colliding energy in 10–40% Au+Au collisions. Results from our model calculation are compared to the STAR [19] and NA49 [51] data. Here, $1.2H_t$ is applied to the baryon number density distribution at $\sqrt{s_{NN}} = 11.5$ and 7.7 GeV.
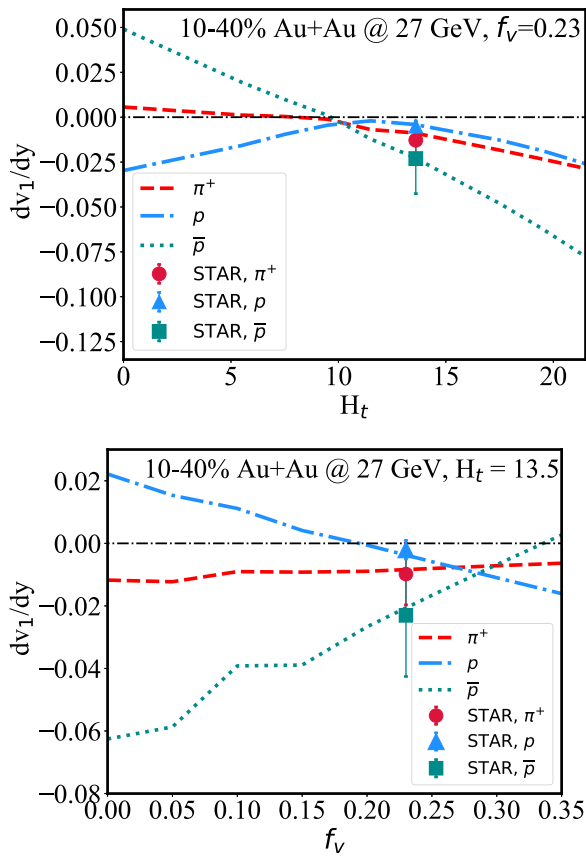

FIG. 6. Upper panel: the slope of the directed flow coefficient dv_1/dy as a function of the tilt parameter H_t when f_v is fixed, in 10–40% Au+Au collisions at $\sqrt{s_{NN}} = 27$ GeV. Lower panel: the slope of the directed flow coefficient as a function of the longitudinal rapidity fraction parameter f_v when H_t is fixed. The experimental data are from the STAR Collaboration [19].

fixed at 0.23. When the longitudinal velocity profile is fixed, we observe the increase of H_t from 0 to 23 leads to a decrease of the slope from positive to negative values for pions and antiprotons. In other words, with finite initial longitudinal flow velocity, the v_1 of pions and antiprotons are positive (negative) in the forward (backward) rapidity region when H_t is small, but flip when H_t is large. Since pions and antiprotons are mainly composed of partons newly produced by nuclear collisions, their v_1 both follow the energy density distribution of the QGP. On the other hand, protons carry baryons deposited by the beam nuclei and therefore their v_1 is significantly affected by the distribution of the initial baryon number density and shows different features compared to pions and antiprotons.

In the lower panel of Fig. 6, we show the slope of $v_1(y)$ as a function f_v when H_t is fixed at 13.5. Compared to Fig. 6, we observe different dependences of dv_1/dy on the medium deformation and its longitudinal flow velocity. While the slopes of pions and antiprotons decrease as the medium becomes more tilted (or H_t increases), the opposite is seen when the longitudinal flow velocity (or f_v) increases.

Figure 6 suggests the sensitivity of the slope of $v_1(y)$ to both the medium geometry and its longitudinal flow profile in the initial state. Here, $H_t = 13.5$ and $f_v = 0.23$ provide the best simultaneous description of the v_1 of pions, protons, and antiprotons at $\sqrt{s_{NN}} = 27$ GeV. Values of these two parameters at other collision energies are constrained in the same way in our work.

D. Global polarization

Apart from the directed flow, the longitudinal flow velocity gradient can also induce polarization of constituent partons inside the QGP via the spin-orbit coupling [50,71,83–89]. It has also been found in Ref. [70] that the global polarization can be affected by the initial geometry of the QGP medium when the same initial longitudinal velocity field is applied. Therefore, due to their similar origins, directed flow and global polarization should be correlated with each other. This correlation was recently investigated in Refs. [50,90]. In this subsection, using the same model setup as previously implemented for studying the hadron v_1, we further explore the global polarization of Λ and $\overline{\Lambda}$ in heavy-ion collisions.

We assume quarks have reached local thermal equilibrium on their freeze-out hypersurface. Meanwhile, the spin of quarks or hadrons are not modified during particlization and resonance decay [63,89,91,92]. Then, the polarization pseudo vector for spin 1/2 fermions can be obtained using the modified Cooper-Frye formalism as [93,94],

$$\mathcal{S}^\mu(\mathbf{p}) = \frac{\int d\Sigma \cdot p \mathcal{J}_5^\mu(p, X)}{2m \int d\Sigma \cdot \mathcal{N}(p, X)}, \quad (28)$$

where $\mathcal{J}_5^\mu$ is the axial charge current density and $\mathcal{N}^\mu(p, X)$ is the number density of fermions in the phase space. Following the quantum kinetic theory [91,92,95], $\mathcal{S}^\mu(\mathbf{p})$ can be decomposed into different sources,

$$\mathcal{S}^\mu(\mathbf{p}) = \mathcal{S}^\mu_{\text{thermal}}(\mathbf{p}) + \mathcal{S}^\mu_{\text{shear}}(\mathbf{p}) + \mathcal{S}^\mu_{\text{accT}}(\mathbf{p})$$
$$+ \mathcal{S}^\mu_{\text{chemical}}(\mathbf{p}) + \mathcal{S}^\mu_{\text{EB}}(\mathbf{p}), \quad (29)$$

where

$$\mathcal{S}^\mu_{\text{thermal}}(\mathbf{p}) = \int d\Sigma^\sigma F_\sigma \epsilon^{\mu\nu\alpha\beta} p_\nu \partial_\alpha \frac{u_\beta}{T},$$

$$\mathcal{S}^\mu_{\text{shear}}(\mathbf{p}) = \int d\Sigma^\sigma F_\sigma \frac{\epsilon^{\mu\nu\alpha\beta} p_\nu u_\beta}{(u \cdot p)T}$$
$$\times p^\rho (\partial_\rho u_\alpha + \partial_\alpha u_\rho - u_\rho D u_\alpha),$$

$$\mathcal{S}^\mu_{\text{accT}}(\mathbf{p}) = -\int d\Sigma^\sigma F_\sigma \frac{\epsilon^{\mu\nu\alpha\beta} p_\nu u_\alpha}{T} \left(D u_\beta - \frac{\partial_\beta T}{T} \right),$$

$$\mathcal{S}^\mu_{\text{chemical}}(\mathbf{p}) = 2 \int d\Sigma^\sigma F_\sigma \frac{1}{(u \cdot p)} \epsilon^{\mu\nu\alpha\beta} p_\alpha u_\beta \partial_\nu \frac{\mu}{T},$$

$$\mathcal{S}^\mu_{\text{EB}}(\mathbf{p}) = 2 \int d\Sigma^\sigma F_\sigma \left[\frac{\epsilon^{\mu\nu\alpha\beta} p_\alpha u_\beta E_\nu}{(u \cdot p)T} + \frac{B^\mu}{T} \right], \quad (30)$$

with

$$F^\mu = \frac{\hbar}{8 m_\Lambda \Phi(\mathbf{p})} p^\mu f_{\text{eq}} (1 - f_{\text{eq}}),$$

$$\Phi(\mathbf{p}) = \int d\Sigma^\mu p_\mu f_{\text{eq}}. \quad (31)$$

The five terms in Eq. (30) represent polarization induced by the thermal vorticity ($\mathcal{S}^\mu_{\text{thermal}}$), the shear tensor ($\mathcal{S}^\mu_{\text{shear}}$), the fluid acceleration minus temperature gradient ($\mathcal{S}^\mu_{\text{accT}}$), the gradient of chemical potential over temperature ($\mathcal{S}^\mu_{\text{chemical}}$), and the external electromagnetic field ($\mathcal{S}^\mu_{\text{EB}}$), respectively. Detailed expressions of these terms can be found in Refs. [63,91,92,95] or derived from the statistic model [96,97] and the Kubo formula [98–101]. Here, S^μ_{shear} and S^μ_{chemical} are also named the shear-induced polarization (SIP) and the baryonic spin Hall effect (SHE) in literature. Since the electromagnetic field decay rapidly in heavy-ion collisions, the $\mathcal{S}^\mu_{\text{EB}}$ term is neglected in our current work.

The average polarization vector in the rest frame of Λ (or $\bar\Lambda$) is then given by

$$\vec{P}^*(\mathbf{p}) = \vec{P}(\mathbf{p}) - \frac{\vec{P}(\mathbf{p}) \cdot \vec{p}}{p^0 (p^0 + m)} \vec{p}, \quad (32)$$

where

$$P^\mu(\mathbf{p}) \equiv \frac{1}{s} \mathcal{S}^\mu(\mathbf{p}), \quad (33)$$

with $s = 1/2$ being the spin of the particle. After averaging over the transverse momentum, one obtains the local polarization as

$$\langle \vec{P}(\phi_p) \rangle = \frac{\int_{y_{\text{min}}}^{y_{\text{max}}} dy \int_{p_{\text{Tmin}}}^{p_{\text{Tmax}}} p_T dp_T [\Phi(\mathbf{p}) \vec{P}^*(\mathbf{p})]}{\int_{y_{\text{min}}}^{y_{\text{max}}} dy \int_{p_{\text{Tmin}}}^{p_{\text{Tmax}}} p_T dp_T \Phi(\mathbf{p})}, \quad (34)$$

in which ϕ_p is the azimuthal angle, and $\Phi(\mathbf{p})$ is an integration on the freeze-out hypersurface defined in Eq. (31). In the present study, the mass of Λ (or $\bar\Lambda$) is set as $m = 1.116$ GeV, and the kinematic regions for analyzing the hyperon polarization are $p_T \in [0.5\,\text{GeV}, 3.0\,\text{GeV}]$ and $y \in [-1, 1]$. Finally, the global polarization of Λ and $\bar\Lambda$ is obtained by further averaging $\vec{P}^*(\mathbf{p})$ over ϕ_p in Eq. (34).

Shown in Fig. 7 is the global polarization of Λ and $\bar\Lambda$ hyperons along the out-of-plane direction as a function of the collision energy in 20–50% Au+Au collisions. Using the
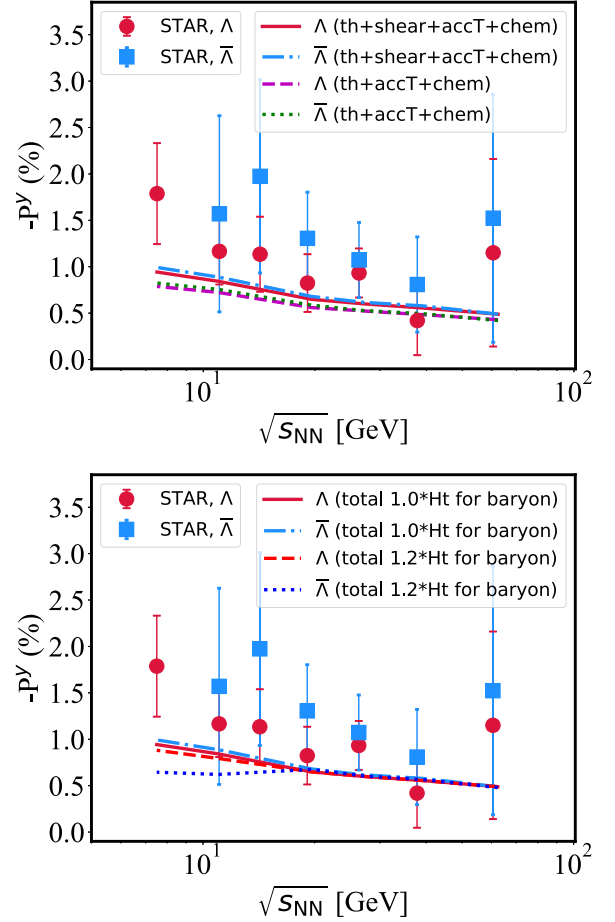

FIG. 7. The global polarization of Λ and $\bar\Lambda$ as a function of the collision energy in 20–50% Au+Au collisions, analyzed within $p_T \in [0.5\,\text{GeV}, 3.0\,\text{GeV}]$, $y \in [-1, 1]$ and compared to the STAR data [102] (rescaled by 0.877 due to the updated hyperon decay parameter [50,103]). In the lower panel, "total" denotes "thermal + shear + accT + chemical" for short.

model parameters H_t and f_v extracted from the directed flow of pions, protons and antiprotons as discussed earlier, our model calculation also provides a reasonable description of the hyperon polarization here. This helps further validate our modeling of the tilted geometry of the QGP together with its longitudinal flow gradient, and also confirms the correlation between the directed flow and the global polarization. We have confirmed that the total amount of polarization presented here is mainly contributed by the thermal vorticity term. The shear tensor relies on the tilted geometry of the medium: a counterclockwise tilt in the reaction plane induces a negative shear tensor, while a clockwise tilt induces a positive shear tensor. Therefore, as shown in the upper panel of Fig. 7, introducing the shear contribution increases the magnitude of $-P_y$. In the lower panel of Fig. 7, we study the effects of the possible larger value of H_t for the net baryon number density than for the energy density at low energies ($\sqrt{s_{NN}} = 11.5$ and 7.7 GeV), as previously suggested by the proton v_1. After introducing this stronger tilt of baryon number density distribution, the global polarization becomes smaller because of

a positive contribution from the chemical term to P_y. We note that the difference between Λ and $\bar{\Lambda}$ polarization relies on both the geometry of baryon distribution and the longitudinal flow velocity. This is why our current result appears different from the earlier study [89] using the same hydrodynamic calculation but different initial condition. The electromagnetic field may cause further difference between their polarization, which has not been included in our current study.

IV. CONCLUSIONS

We have developed an initial condition model for studying the directed flow and global polarization of identified hadrons in heavy-ion collisions across the BES energies. The Glauber model has been extended such that effects of the tilted geometry of both the energy density and the net baryon number density distribution have been included. The initial longitudinal flow velocity profile has also been introduced. By combining this initial condition with a hydrodynamic simulation of the QGP evolution, we have provided a satisfactory description of the transverse momentum spectra of identified particles (π^+, K^+, p, and $\bar{p}$) from $\sqrt{s_{NN}} = 7.7$ to 62.4 GeV. The directed flow coefficients of these identified hadrons, especially the splitting of v_1 between protons and antiprotons, have been investigated in detail.

Our calculation shows the essential role of the tilted medium geometry and the early-time longitudinal flow velocity in generating the directed flow of hadrons. While both the strength of tilt (or the H_t parameter) and the fractional longitudinal momentum deposition (or f_v) become larger at lower collisional energies, they have different impacts on the slope of $v_1(y)$ of different hadron species. An increasing H_t results in a decrease of dv_1/dy around midrapidity for both pions and antiprotons, while an increasing f_v causes their increase. The opposite trend could be seen for protons, which are strongly affected by the baryon number density distribution deposited by the colliding beam. Therefore, a simultaneous comparison of the pion, proton, and antiproton v_1 to their experimental data sets a tight constraint on the inhomogeneous distribution of the initial energy and baryon number density, and the longitudinal flow velocity profile of the nuclear matter created in noncentral heavy-ion collisions. The initial geometry and flow velocity extracted from the hadron v_1 is further tested with the global polarization of Λ and $\bar{\Lambda}$ hyperons that is also affected by the medium geometry and the fluid velocity gradient in the longitudinal direction. Using the same hydrodynamic framework, we obtain a reasonable description of the hyperon polarization across the BES energies, and find that the separation of global polarization between Λ and $\bar{\Lambda}$ could also be sensitive to the tilted geometry of the net baryon number density distribution. Note that the splitting of v_1 between protons and antiprotons is not reflected in a large splitting of the polarization between Λ and $\bar{\Lambda}$ from $\sqrt{s_{NN}} = 7.7$ to 62.4 GeV, implying different sensitivities of these two observables to the baryon number density distribution.

Our study constitutes a step forward in understanding the origin of the splitting of v_1 between different particle species produced in Au+Au collisions at $\sqrt{s_{NN}} = 7.7$–62.4 GeV. While the v_1 of protons and antiprotons is described well for energies $\sqrt{s_{NN}} = 19.6$ GeV and above, additional effects besides the deformed medium geometry and the initial longitudinal flow velocity gradient should be explored for the splitting of v_1 between protons and antiprotons at lower energies. For example, the electromagnetic field produced in noncentral heavy-ion collisions results in directional drift of charged quarks (u, d, s) and therefore different values of v_1 between different final state charged particles. Additionally, the light hadron v_1 can also be affected by the decelerated baryon flow and hadronic cascade after the QGP expansion, especially at lower collision energy [45,49,50]. Therefore, a combination of hydrodynamic model and afterburner hadronic transport is necessary for a better constraint on the initial state. Furthermore, due to the limit of our current smooth initial condition, our calculation is restricted to the rapidity odd component of v_1. The rapidity even component, especially its nontrivial p_T dependence even at midrapidity [104–106], is another interesting topic to investigate after our initialization method is extended to include event-by-event fluctuations. Last but not least, the initial condition and the QGP profile we propose here can be straightforwardly coupled to studies of hard probes in low energy collisions, such as the collective flow of high p_T hadrons and heavy quarks [107] and their correlations [108,109]. These will be addressed in our upcoming efforts.

[1] J.-Y. Ollitrault, Anisotropy as a signature of transverse collective flow, Phys. Rev. D **46**, 229 (1992).

[2] D. H. Rischke, S. Bernard, and J. A. Maruhn, Relativistic hydrodynamics for heavy ion collisions. 1. General aspects and expansion into vacuum, Nucl. Phys. A **595**, 346 (1995).

[3] H. Sorge, Elliptical Flow: A Signature for Early Pressure in Ultrarelativistic Nucleus-Nucleus Collisions, Phys. Rev. Lett. **78**, 2309 (1997).

[4] S. A. Bass, M. Gyulassy, H. Stoecker, and W. Greiner, Signatures of quark gluon plasma formation in high-energy heavy ion collisions: A Critical review, J. Phys. G **25**, R1 (1999).

[5] C. E. Aguiar, Y. Hama, T. Kodama, and T. Osada, Event-by-event fluctuations in hydrodynamical description of heavy ion collisions, Nucl. Phys. A **698**, 639 (2002).

[6] E. Shuryak, Why does the quark gluon plasma at RHIC behave as a nearly ideal fluid? Prog. Part. Nucl. Phys. **53**, 273 (2004).

[7] U. Heinz and R. Snellings, Collective flow and viscosity in relativistic heavy-ion collisions, Annu. Rev. Nucl. Part. Sci. **63**, 123 (2013).

[8] W. Busza, K. Rajagopal, and W. van der Schee, Heavy ion collisions: The big picture, and the big questions, Annu. Rev. Nucl. Part. Sci. **68**, 339 (2018).

[9] Y. Aoki, G. Endrodi, Z. Fodor, S. D. Katz, and K. K. Szabo, The order of the quantum chromodynamics transition predicted by the standard model of particle physics, Nature (London) **443**, 675 (2006).

[10] *The CBM Physics Book: Compressed Baryonic Matter in Laboratory Experiments*, edited by B. Friman, C. Hohne, J. Knoll, S. Leupold, J. Randrup, R. Rapp, and P. Senger, Lecture Notes in Physics Vol. 814 (Springer, Berlin, 2011).

[11] D. H. Rischke, Y. Pürsün, J. A. Maruhn, H. Stoecker, and W. Greiner, The Phase transition to the quark-gluon plasma and its effects on hydrodynamic flow, Acta Phys. Hung. A **1**, 309 (1995).

[12] G. Odyniec, Future of the beam energy scan program at RHIC, EPJ Web Conf. **95**, 03027 (2015).

[13] V. Kekelidze, A. Kovalenko, R. Lednicky, V. Matveev, I. Meshkov, A. Sorin, and G. Trubnikov, Prospects for the dense baryonic matter research at NICA, Nucl. Phys. A **956**, 846 (2016).

[14] H. Sako *et al.*, Studies of high density baryon matter with high intensity heavy-ion beams at J-PARC, Nucl. Phys. A **956**, 850 (2016).

[15] J. Barrette *et al.*, Proton and pion production relative to the reaction plane in Au + Au collisions at AGS energies, Phys. Rev. C **56**, 3254 (1997).

[16] H. Liu *et al.*, Sideward Flow in Au+Au Collisions between 2A and 8A GeV, Phys. Rev. Lett. **84**, 5488 (2000).

[17] T. Ablyazimov *et al.*, Challenges in QCD matter physics–The scientific programme of the Compressed Baryonic Matter experiment at FAIR, Eur. Phys. J. A **53**, 60 (2017).

[18] M. Abdallah *et al.*, Cumulants and correlation functions of net-proton, proton, and antiproton multiplicity distributions in Au+Au collisions at energies available at the BNL Relativistic Heavy Ion Collider, Phys. Rev. C **104**, 024902 (2021).

[19] L. Adamczyk *et al.*, Beam-Energy Dependence of the Directed Flow of Protons, Antiprotons, and Pions in Au+Au Collisions, Phys. Rev. Lett. **112**, 162301 (2014).

[20] L. Adamczyk *et al.*, Beam-Energy Dependence of Directed Flow of Λ, $\bar{\Lambda}$, $K^{\pm}$, K_s^0 and ϕ in Au+Au Collisions, Phys. Rev. Lett. **120**, 062301 (2018).

[21] M. S. Abdallah *et al.*, Light nuclei collectivity from $\sqrt{s_{NN}}$ = 3 GeV Au+Au collisions at RHIC, Phys. Lett. B **827**, 136941 (2022).

[22] X. Luo, S. Shi, N. Xu, and Y. Zhang, A study of the properties of the QCD phase diagram in high-energy nuclear collisions, Particles **3**, 278, (2020).

[23] A. Bzdak, S. Esumi, V. Koch, J. Liao, M. Stephanov, and N. Xu, Mapping the phases of quantum chromodynamics with Beam Energy Scan, Phys. Rep. **853**, 1 (2020).

[24] K.-J. Sun, F. Li, and C. M. Ko, Effects of QCD critical point on light nuclei production, Phys. Lett. B **816**, 136258 (2021).

[25] L. Adamczyk *et al.*, Beam Energy Dependence of Jet-Quenching Effects in Au+Au Collisions at $\sqrt{s_{NN}}$ = 7.7, 11.5, 14.5, 19.6, 27, 39, and 62.4 GeV, Phys. Rev. Lett. **121**, 032301 (2018).

[26] J. Wu, S. Cao, and F. Li, Partonic critical opalescence and its impact on the jet quenching parameter $\hat{q}$, arXiv:2208.14297.

[27] S. Voloshin and Y. Zhang, Flow study in relativistic nuclear collisions by Fourier expansion of azimuthal particle distributions, Z. Phys. C **70**, 665 (1996).

[28] A. Bilandzic, R. Snellings, and S. Voloshin, Flow analysis with cumulants: Direct calculations, Phys. Rev. C **83**, 044913 (2011).

[29] J. Adams *et al.*, Azimuthal anisotropy in Au+Au collisions at $\sqrt{s_{NN}}$ = 200GeV, Phys. Rev. C **72**, 014904 (2005).

[30] J. Adam *et al.*, First Observation of the Directed Flow of D^0 and $\bar{D}^0$ in Au+Au Collisions at $\sqrt{s_{NN}}$ = 200 GeV, Phys. Rev. Lett. **123**, 162301 (2019).

[31] S. Acharya *et al.*, Probing the Effects of Strong Electromagnetic Fields with Charge-Dependent Directed Flow in Pb-Pb Collisions at the LHC, Phys. Rev. Lett. **125**, 022301 (2020).

[32] J. Adam *et al.*, Bulk properties of the system formed in Au+Au collisions at $\sqrt{s_{NN}}$ =14.5 GeV at the BNL STAR detector, Phys. Rev. C **101**, 024905 (2020).

[33] M. Gyulassy, K. A. Frankel, and H. Stoecker, Do nuclei flow at high-energies? Phys. Lett. B **110**, 185 (1982).

[34] H. A. Gustafsson *et al.*, Collective Flow Observed in Relativistic Nuclear Collisions, Phys. Rev. Lett. **52**, 1590 (1984).

[35] M. A. Lisa, U. W. Heinz, and U. A. Wiedemann, Tilted pion sources from azimuthally sensitive HBT interferometry, Phys. Lett. B **489**, 287 (2000).

[36] S. S. Adler *et al.*, Elliptic Flow of Identified Hadrons in Au + Au Collisions at $\sqrt{s_{NN}}$ = 200 GeV, Phys. Rev. Lett. **91**, 182301 (2003).

[37] K. Aamodt *et al.*, Elliptic Flow of Charged Particles in Pb-Pb Collisions at 2.76 TeV, Phys. Rev. Lett. **105**, 252302 (2010).

[38] S. Chatrchyan *et al.*, Measurement of the elliptic anisotropy of charged particles produced in PbPb collisions at $\sqrt{s_{NN}}$ = 2.76 TeV, Phys. Rev. C **87**, 014902 (2013).

[39] Y. Nara, H. Niemi, A. Ohnishi, and H. Stöcker, Examination of directed flow as a signature of the softest point of the equation of state in QCD matter, Phys. Rev. C **94**, 034906 (2016).

[40] S. Chatterjee and P. Bożek, Large Directed Flow of Open Charm Mesons Probes the Three Dimensional Distribution of Matter in Heavy Ion Collisions, Phys. Rev. Lett. **120**, 192301 (2018).

[41] S. Singha, P. Shanmuganathan, and D. Keane, The first moment of azimuthal anisotropy in nuclear collisions from AGS to LHC energies, Adv. High Energy Phys. **2016**, 2836989 (2016).

[42] C. Zhang, J. Chen, X. Luo, F. Liu, and Y. Nara, Beam energy dependence of the squeeze-out effect on the directed and elliptic flow in Au + Au collisions in the high baryon density region, Phys. Rev. C **97**, 064913 (2018).

[43] C.-Q. Guo, C.-J. Zhang, and J. Xu, Revisiting directed flow in relativistic heavy-ion collisions from a multiphase transport model, Eur. Phys. J. A **53**, 233 (2017).

[44] T. Parida and S. Chatterjee, Splitting of elliptic flow in a tilted fireball, Phys. Rev. C **106**, 044907 (2022).

[45] P. Bozek, Splitting of proton-antiproton directed flow in relativistic heavy-ion collisions, Phys. Rev. C **106**, L061901 (2022).

[46] P. Bozek, Flow and interferometry in 3+1 dimensional viscous hydrodynamics, Phys. Rev. C **85**, 034901 (2012).

[47] Z.-F. Jiang, S. Cao, X.-Y. Wu, C. B. Yang, and B.-W. Zhang, Longitudinal distribution of initial energy density and directed flow of charged particles in relativistic heavy-ion collisions, Phys. Rev. C **105**, 034901 (2022).

[48] Z.-F. Jiang, C. B. Yang, and Q. Peng, Directed flow of charged particles within idealized viscous hydrodynamics at energies available at the BNL Relativistic Heavy Ion Collider and at the CERN Large Hadron Collider, Phys. Rev. C **104**, 064903 (2021).

[49] C. Shen and S. Alzhrani, Collision-geometry-based 3D initial condition for relativistic heavy-ion collisions, Phys. Rev. C **102**, 014909 (2020).

[50] S. Ryu, V. Jupic, and C. Shen, Probing early-time longitudinal dynamics with the Λ hyperon's spin polarization in relativistic heavy-ion collisions, Phys. Rev. C **104**, 054908 (2021).

[51] C. Alt *et al.*, Directed and elliptic flow of charged pions and protons in Pb + Pb collisions at 40*A* and 158*A* GeV, Phys. Rev. C **68**, 034903 (2003).

[52] J. Y. Chen, J. X. Zuo, X. Z. Cai, F. Liu, Y. G. Ma, and A. H. Tang, Energy dependence of directed flow in Au+Au collisions from a multiphase transport model, Phys. Rev. C **81**, 014904 (2010).

[53] J. Steinheimer, J. Auvinen, H. Petersen, M. Bleicher, and H. Stöcker, Examination of directed flow as a signal for a phase transition in relativistic nuclear collisions, Phys. Rev. C **89**, 054913 (2014).

[54] V. P. Konchakovski, W. Cassing, Yu. B. Ivanov, and V. D. Toneev, Examination of the directed flow puzzle in heavy-ion collisions, Phys. Rev. C **90**, 014903 (2014).

[55] Y. Guo, F. Liu, and A. Tang, Directed flow of transported and nontransported protons in Au+Au collisions from an ultrarelativistic quantum molecular dynamics model, Phys. Rev. C **86**, 044901 (2012).

[56] Yu. B. Ivanov and A. A. Soldatov, Directed flow indicates a cross-over deconfinement transition in relativistic nuclear collisions, Phys. Rev. C **91**, 024915 (2015).

[57] T. Parida and S. Chatterjee, Directed flow of light flavor hadrons for Au+Au collisions at $\sqrt{s_{NN}} = 7.7$–200 GeV, arXiv:2211.15659.

[58] T. Parida and S. Chatterjee, Directed flow in a baryonic fireball, arXiv:2211.15729.

[59] L. Du, C. Shen, S. Jeon, and C. Gale, Probing initial baryon stopping and equation of state with rapidity-dependent directed flow of identified particles, arXiv:2211.16408.

[60] L.-G. Pang, H. Petersen, Q. Wang, and X.-N. Wang, Vortical Fluid and Λ Spin Correlations in High-Energy Heavy-Ion Collisions, Phys. Rev. Lett. **117**, 192301 (2016).

[61] L.-G. Pang, H. Petersen, and X.-N. Wang, Pseudorapidity distribution and decorrelation of anisotropic flow within the open-computing-language implementation CLVisc hydrodynamics, Phys. Rev. C **97**, 064918 (2018).

[62] X.-Y. Wu, L.-G. Pang, G.-Y. Qin, and X.-N. Wang, Longitudinal fluctuations and decorrelations of anisotropic flows at energies available at the CERN Large Hadron Collider and at the BNL Relativistic Heavy Ion Collider, Phys. Rev. C **98**, 024913 (2018).

[63] X.-Y. Wu, G.-Y. Qin, L.-G. Pang, and X.-N. Wang, (3+1)-D viscous hydrodynamics at finite net baryon density: Identified particle spectra, anisotropic flows, and flow fluctuations across energies relevant to the beam-energy scan at RHIC, Phys. Rev. C **105**, 034909 (2022).

[64] P. Bozek and I. Wyskiel, Directed flow in ultrarelativistic heavy-ion collisions, Phys. Rev. C **81**, 054902 (2010).

[65] C. Loizides, J. Kamin, and D. d'Enterria, Improved Monte Carlo Glauber predictions at present and future nuclear colliders, Phys. Rev. C **97**, 054910 (2018); **99**, 019901(E) (2019).

[66] M. Abdallah *et al.*, Search for the chiral magnetic effect with isobar collisions at $\sqrt{s_{NN}} = 200$ GeV by the STAR Collaboration at the BNL Relativistic Heavy Ion Collider, Phys. Rev. C **105**, 014901 (2022).

[67] Z.-F. Jiang, S. Cao, W.-J. Xing, X.-Y. Wu, C. B. Yang, and B.-W. Zhang, Probing the initial longitudinal density profile and electromagnetic field in ultrarelativistic heavy-ion collisions with heavy quarks, Phys. Rev. C **105**, 054907 (2022).

[68] C. Shen and B. Schenke, Dynamical initial state model for relativistic heavy-ion collisions, Phys. Rev. C **97**, 024907 (2018).

[69] A. Bialas and M. Jezabek, Bremsstrahlung from color charges as a source of soft particle production in hadronic collisions, Phys. Lett. B **590**, 233 (2004).

[70] X. Li, Z.-F. Jiang, S. Cao, and J. Deng, Evolution of global polarization in relativistic heavy-ion collisions within a perturbative approach, Eur. Phys. J. C **83**, 96 (2023).

[71] S. Alzhrani, S. Ryu, and C. Shen, Λ spin polarization in event-by-event relativistic heavy-ion collisions, Phys. Rev. C **106**, 014905 (2022).

[72] A. Rybicki and A. Szczurek, Spectator induced electromagnetic effect on directed flow in heavy ion collisions, Phys. Rev. C **87**, 054909 (2013).

[73] Z. F. Jiang, D. She, C. B. Yang, and D. Hou, Perturbation solutions of relativistic viscous hydrodynamics for longitudinally expanding fireballs, Chin. Phys. C **44**, 084107 (2020).

[74] Z. F. Jiang, C. B. Yang, C. Ding, and X.-Y. Wu, Pseudo-rapidity distribution from a perturbative solution of viscous hydrodynamics for heavy ion collisions at RHIC and LHC, Chin. Phys. C **42**, 123103 (2018).

[75] G. S. Denicol, H. Niemi, E. Molnar, and D. H. Rischke, Derivation of transient relativistic fluid dynamics from the Boltzmann equation, Phys. Rev. D **85**, 114047 (2012); **91**, 039902(E) (2015).

[76] P. Romatschke, New developments in relativistic viscous hydrodynamics, Int. J. Mod. Phys. E **19**, 1 (2010).

[77] P. Romatschke and U. Romatschke, *Relativistic Fluid Dynamics In and Out of Equilibrium*, Cambridge Monographs on Mathematical Physics (Cambridge University Press, Cambridge, 2019).

[78] Y. Akamatsu, M. Asakawa, T. Hirano, M. Kitazawa, K. Morita, K. Murase, Y. Nara, C. Nonaka, and A. Ohnishi, Dynamically integrated transport approach for heavy-ion collisions at high baryon density, Phys. Rev. C **98**, 024909 (2018).

[79] G. S. Denicol, C. Gale, S. Jeon, A. Monnai, B. Schenke, and C. Shen, Net baryon diffusion in fluid dynamic simulations of relativistic heavy-ion collisions, Phys. Rev. C **98**, 034916 (2018).

[80] A. Monnai, B. Schenke, and C. Shen, Equation of state at finite densities for QCD matter in nuclear collisions, Phys. Rev. C **100**, 024907 (2019).

[81] A. Monnai, B. Schenke, and C. Shen, QCD equation of state at finite chemical potentials for relativistic nuclear collisions, Int. J. Mod. Phys. A **36**, 2130007 (2021).

[82] M. McNelis and U. Heinz, Modified equilibrium distributions for Cooper-Frye particlization, Phys. Rev. C **103**, 064903 (2021).

[83] Z.-T. Liang and X.-N. Wang, Globally Polarized Quark-Gluon Plasma in Noncentral $A + A$ Collisions, Phys. Rev. Lett. **94**, 102301 (2005); **96**, 039901(E) (2006).

[84] Z.-T. Liang and X.-N. Wang, Spin alignment of vector mesons in non-central A+A collisions, Phys. Lett. B **629**, 20 (2005).

[85] X.-G. Huang, P. Huovinen, and X.-N. Wang, Quark polarization in a viscous quark-gluon plasma, Phys. Rev. C **84**, 054910 (2011).

[86] L. Adamczyk *et al.*, Global Λ hyperon polarization in nuclear collisions: evidence for the most vortical fluid, Nature (London) **548**, 62 (2017).

[87] H. Li, X.-L. Xia, X.-G. Huang, and H. Z. Huang, Global spin polarization of multistrange hyperons and feed-down effect in heavy-ion collisions, Phys. Lett. B **827**, 136971 (2022).

[88] Y. Guo, S. Shi, S. Feng, and J. Liao, Magnetic Field Induced Polarization difference between hyperons and anti-hyperons, Phys. Lett. B **798**, 134929 (2019).

[89] X.-Y. Wu, C. Yi, G.-Y. Qin, and S. Pu, Local and global polarization of Λ hyperons across RHIC-BES energies: The roles of spin hall effect, initial condition, and baryon diffusion, Phys. Rev. C **105**, 064909 (2022).

[90] Yu. B. Ivanov and A. A. Soldatov, Correlation between global polarization, angular momentum, and flow in heavy-ion collisions, Phys. Rev. C **102**, 024916 (2020).

[91] C. Yi, S. Pu, and D.-L. Yang, Reexamination of local spin polarization beyond global equilibrium in relativistic heavy ion collisions, Phys. Rev. C **104**, 064901 (2021).

[92] C. Yi, S. Pu, J.-H. Gao, and D.-L. Yang, Hydrodynamic helicity polarization in relativistic heavy ion collisions, Phys. Rev. C **105**, 044911 (2022).

[93] F. Becattini, V. Chandra, L. Del Zanna, and E. Grossi, Relativistic distribution function for particles with spin at local thermodynamical equilibrium, Ann. Phys. (NY) **338**, 32 (2013).

[94] R.-h. Fang, L.-g. Pang, Q. Wang, and X.-n. Wang, Polarization of massive fermions in a vortical fluid, Phys. Rev. C **94**, 024904 (2016).

[95] Y. Hidaka, S. Pu, and D.-L. Yang, Nonlinear responses of chiral fluids from kinetic theory, Phys. Rev. D **97**, 016004 (2018).

[96] F. Becattini, M. Buzzegoli, and A. Palermo, Spin-thermal shear coupling in a relativistic fluid, Phys. Lett. B **820**, 136519 (2021).

[97] F. Becattini, M. Buzzegoli, G. Inghirami, I. Karpenko, and A. Palermo, Local Polarization and Isothermal Local Equilibrium in Relativistic Heavy Ion Collisions, Phys. Rev. Lett. **127**, 272302 (2021).

[98] S. Y. F. Liu and Y. Yin, Spin Hall effect in heavy-ion collisions, Phys. Rev. D **104**, 054043 (2021).

[99] S. Y. F. Liu and Y. Yin, Spin polarization induced by the hydrodynamic gradients, J. High Energy Phys. 07 (2021) 188.

[100] B. Fu, S. Y. F. Liu, L. Pang, H. Song, and Y. Yin, Shear-Induced Spin Polarization in Heavy-Ion Collisions, Phys. Rev. Lett. **127**, 142301 (2021).

[101] B. Fu, L. Pang, H. Song, and Y. Yin, Signatures of the spin Hall effect in hot and dense QCD matter, arXiv:2201.12970.

[102] M. S. Abdallah *et al.*, Global Λ-hyperon polarization in Au+Au collisions at $\sqrt{s_{NN}} = 3$ GeV, Phys. Rev. C **104**, L061901 (2021).

[103] P. A. Zyla *et al.*, Review of particle physics, Prog. Theor. Exp. Phys. **2020**, 083C01.

[104] D. Teaney and L. Yan, Triangularity and dipole asymmetry in heavy ion collisions, Phys. Rev. C **83**, 064904 (2011).

[105] M. Luzum and J.-Y. Ollitrault, Directed Flow at Midrapidity in Heavy-Ion Collisions, Phys. Rev. Lett. **106**, 102301 (2011).

[106] C. Gale, S. Jeon, B. Schenke, P. Tribedy, and R. Venugopalan, Event-by-Event Anisotropic Flow in Heavy-ion Collisions from Combined Yang-Mills and Viscous Fluid Dynamics, Phys. Rev. Lett. **110**, 012302 (2013).

[107] Z.-F. Jiang, S. Cao, W.-J. Xing, X. Li, and B.-W. Zhang, Interactions between heavy quarks and tilted QGP fireballs in 200 A GeV Au+Au collisions, Chin. Phys. C **47**, 024107 (2023).

[108] L. Ma, X. Dong, H.-Z. Huang, and Y.-G. Ma, Study of a background reconstruction method for the measurement of D-meson azimuthal angular correlations, Nucl. Sci. Technol. **32**, 61 (2021).

[109] S. Acharya *et al.*, Azimuthal correlations of prompt D mesons with charged particles in pp and p–Pb collisions at $\sqrt{s_{NN}} = $ 5.02 TeV, Eur. Phys. J. C **80**, 979 (2020).